Propagation of coherent longitudinal and shear waves in two-dimensional elastic media with randomly distributed resonant cavities

Tony Valier-Brasier,[*] Adrien Rohfritsch, Jean-Marc Conoir, and Régis Marchiano
Sorbonne Université, CNRS, Institut Jean Le Rond d'Alembert, UMR 7190, 4 Place Jussieu, Paris, F-75005, France

Propagation of coherent elastic waves in solids containing randomly distributed resonant cylindrical cavities is studied numerically and experimentally. This work focuses especially on the case of water-filled cavities in aluminum alloys, which exhibit numerous Mie resonances in the frequency range investigated. Coherent wave measurements are performed in transmission at normal incidence for longitudinal waves and at oblique incidence beyond the critical angle for shear waves. Experimental observations are completed by numerical simulations made with an in-house code called MuScat adapted to the solid matrix case with wave conversions at the surface of each scatterer. The effective wave numbers obtained experimentally and numerically are compared with those predicted by statistical models based on the multiple scattering theory. Remarkable agreements between theoretical, numerical, and experimental results are obtained up to a concentration of 9.9% of cylinders.

I. INTRODUCTION

Multiple scattering of elastic waves in solid media is a topic of fundamental interest, especially in geophysics, nondestructive testing (NDT), and medical imaging. In NDT, this may concern the propagation of elastic waves in fiber-reinforced composites [1–3] as well as in elastic metamaterials [4,5]. However, the topic of the multiple scattering by discrete scatterers has been less studied in solid media, compared to fluid matrices. The main difference is the existence of wave conversions that occur at the surface of each scatterer, leading to the coupled propagation of bulk longitudinal and shear waves. This coupling affects the propagation of both longitudinal and shear waves and it cannot be neglected, especially in the presence of resonances.

Lot of studies have been dedicated to the propagation in phononic crystals where the periodical arrangement induces interesting properties for the propagation. In comparison less attention has been paid to randomly distributed scatterers in a solid matrix. Extending the classical Fikioris and Waterman's multiple scattering theory for scalar waves, Conoir and Norris [6] (CN model hereafter) have developed a statistical model to get the properties of coherent waves in elastic multiple scattering medium. This model outlines the importance of the wave conversions even at low concentration. It has been validated by numerical studies [7,8] and experiments [8] in the case of nonresonant scatterers. Chekroun *et al.* [7] compared the results of the CN model to numerically estimated effective wave numbers (direct resolution of the equations of elastodynamics) of coherent elastic waves propagating in concrete materials up to a concentration $\phi = 25\%$ of scatterers whose properties were close to the matrix ones. Yu *et al.* measured the effective wave number of coherent longitudinal waves propagating in a resin containing randomly distributed

aluminum rods [8]. For this configuration, the elasticity and mass density contrasts between the two constituents being small, the scattering effects are relatively weak, allowing them to study high concentrations of scatterers up to 40%. Recently, shear coherent waves have been measured in epoxy samples containing hard dense spheres that exhibit strong dipolar subwavelength resonances [9]. No numerical or experimental studies address the effects of Mie scatterers in a solid matrix, although it has been shown they have a strong effect on coherent acoustic waves [10–12].

The contributions of this work are, on one hand, to characterize both the coherent longitudinal and shear waves in a solid medium and, on the other hand, to observe the impact of Mie resonances on these coherent waves. Analyses are made on aluminum alloys containing water-filled cavities. Parameters of the longitudinal and shear coherent waves are measured by transmission experiments through samples. Experiments are performed at normal incidence for longitudinal waves and at oblique incidence beyond the critical angle for shear waves. Numerical simulations are then performed in order to highlight the influence of wave conversions on coherent waves.

The paper is structured as follows. In Sec. II, the scattering of elastic waves by a single water-filled cavity in an aluminum alloy is presented in order to identify the Mie resonances due to the propagation of circumferential waves around the cavities. In Sec. III, the experimental setup used to generate and to measure coherent elastic waves is described. The numerical model used to simulate the propagation is presented in Sec. IV and its detailed derivation is given in the Appendix. Then the propagation is studied for an elastic coherent longitudinal wave in Sec. V and for a coherent shear wave in Sec. VI.

II. SCATTERING BY A SINGLE WATER-FILLED CAVITY IN AN ALUMINUM ALLOY

Before addressing the propagation of elastic waves in multiple scattering media, the scattering of elastic waves by a

[*]tony.valier-brasier@sorbonne-universite.fr
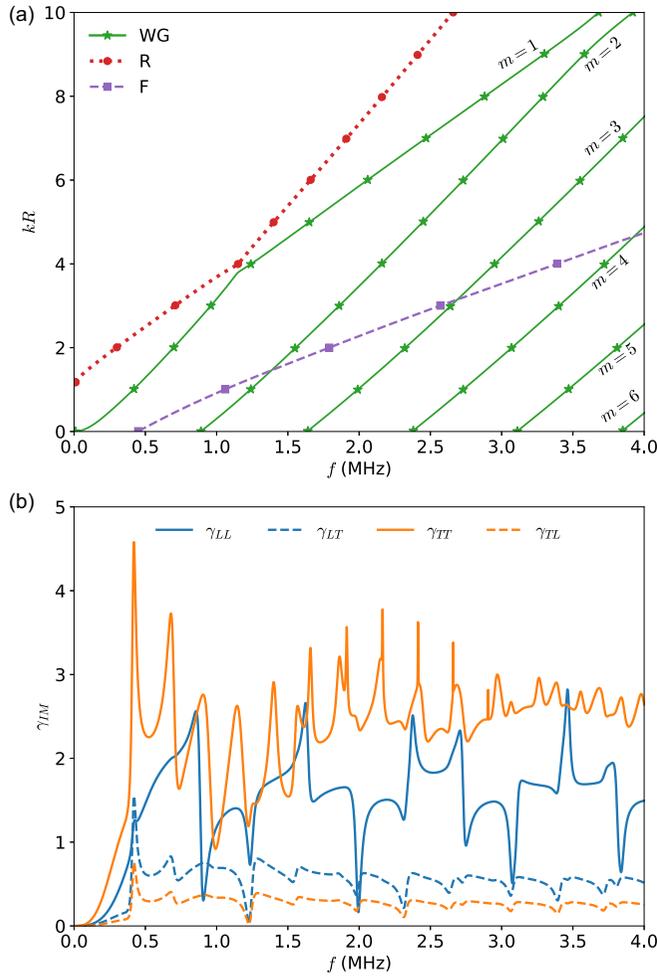
054310-1

FIG. 1. (a) Dispersion curves of the whispering gallery waves and the Rayleigh and Franz waves as a function of frequency. Markers correspond to resonance frequencies of circumferential waves. (b) Normalized scattering cross sections of elastic waves as a function of frequency.

single cavity must be studied. In this paper we focus our analysis on the case of water-filled cavities which exhibit many Mie resonances due to circumferential waves [13,14].

The dispersion curves of circumferential waves propagating around a cylindrical water-filled cavity in an elastic host are calculated by using the modeling of Hassan and Nagy [15]. The aluminum alloy is characterized by the Lamé constants $\lambda = 58$ GPa and $\mu = 26.4$ GPa and the mass density $\rho = 2800$ kg/m^3. The radius of the cavity is $R = 1$ mm, the sound velocity in water is $c_F = 1480$ m/s, and the density is $\rho_F = 1000$ kg/m^3. Figure 1(a) shows the dispersion curves of the first whispering gallery waves (WGs) $m = 1$ to 6, the Rayleigh wave (R), and the Franz wave (F) as a function of the frequency f. Each integer value $kR = n$, represented by markers in Fig. 1(a), corresponds to a resonance. In the frequency range investigated experimentally, i.e., $f \in [0, 5\text{--}4]$ MHz, many resonances can therefore be excited. The resonances for $n = 0$ are associated with pure radial compressional motions and those for values $n \geqslant 1$ correspond to the number n of rounds of circumferential waves around the cavity. These resonances result from the propagation of circumferential waves

around the cavity, clockwise and counterclockwise, that superpose in phase after each period, leading to a standing wave.

In order to determine which resonances are excited and impact coherent waves, the scattering cross sections are evaluated. The scattering cross sections normalized by the geometric section of the scatterer are given by [16]

$$\gamma_{IM} = \frac{2}{k_I R} \sum_{n=-\infty}^{\infty} \left| T_n^{IM} \right|^2, \qquad (1)$$

where T_n^{IM} is the scattering coefficient of the mode n for an incident wave I (with $I = L, T$) and a scattered wave M (with $M = L, T$). The calculations of these coefficients are presented in Ref. [17]. The wave numbers $k_L = \omega/c_L$ and $k_T = \omega/c_T$ are related to angular frequency ω and velocities of bulk longitudinal and shear waves that are given by

$$c_L = \sqrt{\frac{\lambda + 2\mu}{\rho}} \quad \text{and} \quad c_T = \sqrt{\frac{\mu}{\rho}}. \qquad (2)$$

The normalized scattering cross sections γ_{IM} of elastic waves are plotted as a function of frequency in Fig. 1(b). The parameters γ_{LT} and γ_{TL}, which quantify the wave conversions, are generally smaller than γ_{LL} and γ_{TT}, respectively. However, at some resonances γ_{LT} is similar and even superior to γ_{LL}, implying that the conversions between longitudinal and shear waves can be important.

It is difficult to link the peaks of the scattering cross sections to resonance frequencies appearing in dispersion curves. To achieve this, the contribution of each mode n to the scattering cross sections γ_{LL} and γ_{TT} is plotted in Fig. 2 as a function of frequency. Markers correspond to resonance frequencies appearing in Fig. 1(a). Figure 2 clearly shows the influence of the resonances of the whispering gallery waves $m = 1$ to 6 on γ_{LL} and γ_{TT}. For these waves, each peak or dip on the scattering cross sections correspond to a resonance. Only the first resonance of the Franz wave seems to be excited and to have an influence on the mode $n = 0$. This wave being very attenuated, the other resonances are not observed. The resonances of the Rayleigh waves are excited only in the case of a shear incident wave. This last point is easily explained by the fact that the Rayleigh wave polarization is strongly transverse.

III. EXPERIMENTAL SETUP

We propose to measure coherent elastic waves through transmission experiments. The main difficulty is to design reproducible measurements with shear waves. To achieve this, experiments are done at oblique incidence beyond the critical angle for shear waves and at normal incidence for longitudinal waves.

The samples are aluminum alloy 2017A plates of thickness 50 mm and widths H and h_t as shown in Fig. 3. A layer of width h_t and thickness h contains a monodisperse and random distribution of circular holes of radius $R = 1$ mm. Three samples are studied in the following with different parameters given in Table I. The number of water-filled cavities N_p is
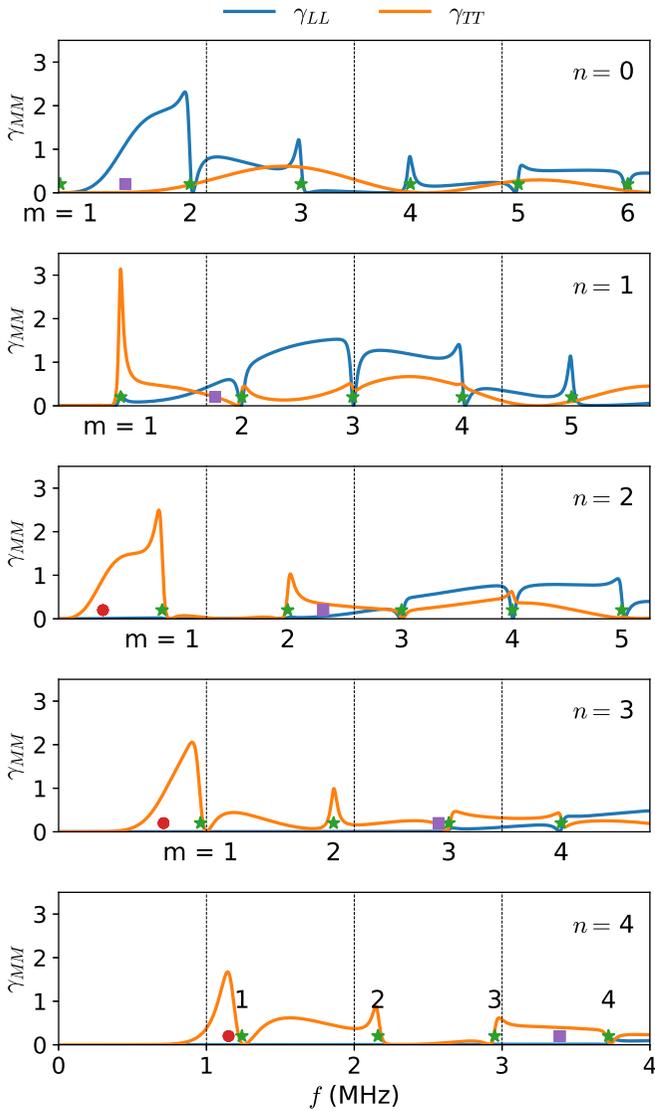
FIG. 2. Contributions of each mode to the normalized scattering cross sections γ_{LL} and γ_{TT} as a function of frequency. Stars correspond to resonance frequencies of whispering gallery waves, disks to those of the Rayleigh wave, and squares to those of the Franz wave.
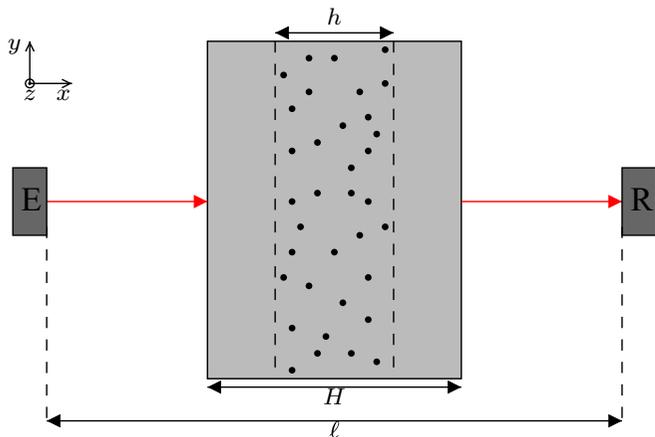

FIG. 3. Scheme of a sample of thickness H. The scatterers are randomly distributed within a layer of thickness h.

TABLE I. Dimensions of samples and parameters of the distributions.

Sample	H (mm)	h (mm)	h_t (mm)	N_p	ϕ (%)	b/R
1	80	30	145	72	5	3
2	60	30	145	143	9.9	4.75
3	80	20	100	50	7.1	4

related to the concentration ϕ by

$$\phi = \frac{N_p \pi R^2}{h h_t}. \qquad (3)$$

Samples are immersed in a water tank and can be translated laterally, i.e., perpendicularly to the acoustic axis. A pair of identical piezoelectric transducers having central frequency $f_c = 2.25$ MHz and diameter $D = 1/2$ in. is used, which allows us to reliably cover the frequency range [0.5–4] MHz. The horizontal distance between the transmitter and receiver transducers is noted ℓ. The nearest surface of the sample to the emitter is located in the far field of the emitter in order to be probed with plane waves. The receiver is facing the emitter and located close to the sample (i.e., ≈ 30 mm away) in order to avoid possible diffraction effects by the bottom and top interfaces of the sample, due to the beam divergence at low frequency.

The distributions of scatterers of the three samples are shown in Fig. 4. Samples 1 and 2 are used for normal incidence measurements and sample 3 for the oblique incidence. For sample 1, the exclusion distance between two scatterers is $b = 3R$, implying that the constraints due to short range correlations are weak for the concentration $\phi = 5\%$. On the
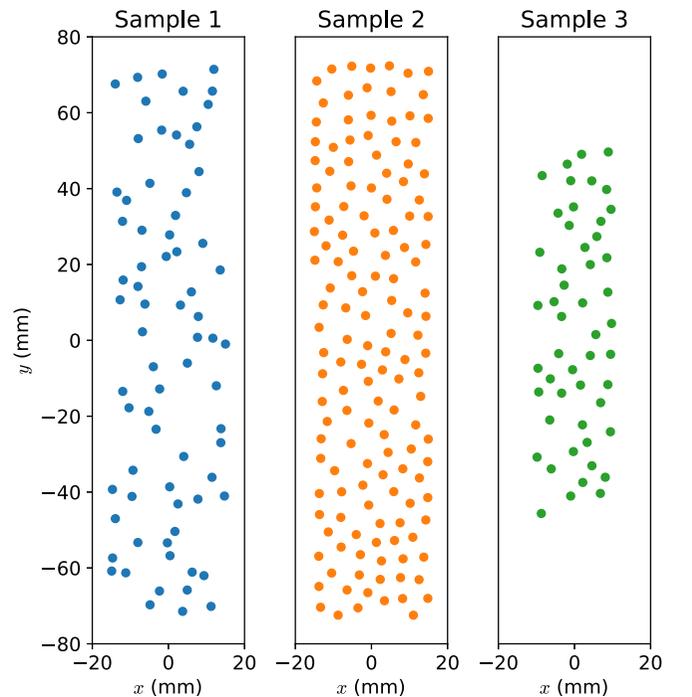

FIG. 4. Distributions of scatterers of the three samples.

contrary, for sample 2, the exclusion distance is $b = 4.75R$ and the concentration $\phi = 9.9\%$, short range correlations between scatterers are strong. This can be seen in Fig. 4 where the holes are more uniformly organized than in sample 1.

IV. NUMERICAL MODEL OF THE ELASTIC WAVE PROPAGATION IN SOLID MULTIPLE SCATTERING MEDIA

Between statistical multiple scattering models, which are intrinsically limited by the concentration and the geometry of the cluster of cylinders, and the direct resolution of the equations of elastodynamics, which require important numerical resources especially when statistics are required as with coherent waves, there is an intermediate stage by considering the resolution of multiple scattering equations [18]. Rohfritsch *et al.* have recently proposed to simulate the propagation of acoustic waves in a fluid containing parallel infinite cylinders with a method called MuScat for multiple scattering [19]. This in-house numerical tool allows us to consider a very large number of cylinders whatever the concentration and the position of scatterers. This has been used later to highlight the influence of the spatial correlations between scatterers on the coherent acoustic waves [20] and to study the acoustic wave propagation in stealth hyperuniform distributions of cylinders [21]. Nevertheless, in these previous studies this software was restricted to acoustic waves since conversions were not taken into account. In this paper we propose to extend the MuScat code to host solids and thus to take into account both longitudinal and shear waves and their conversions by following the method developed by Mei *et al.* [22] who investigated phononic crystals. The detailed derivation of the multiple scattering equations with waves conversion at the surface of each scatterer is given in the Appendix A. It yields to a large linear system:

$$\begin{pmatrix} \mathcal{I} - \mathcal{T}^{LL}\mathcal{M}^L & -\mathcal{T}^{TL}\mathcal{M}^T \\ -\mathcal{T}^{LT}\mathcal{M}^L & \mathcal{I} - \mathcal{T}^{TT}\mathcal{M}^T \end{pmatrix} \begin{pmatrix} \mathcal{B}^L \\ \mathcal{B}^T \end{pmatrix}$$
$$= \begin{pmatrix} \mathcal{T}^{LL}\mathcal{F}^L + \mathcal{T}^{TL}\mathcal{F}^T \\ \mathcal{T}^{LT}\mathcal{F}^L + \mathcal{T}^{TT}\mathcal{F}^T \end{pmatrix}, \quad (4)$$

where the unknown vectors $\mathcal{B}^L$ and $\mathcal{B}^T$ are, respectively, the amplitudes of the cylindrical harmonics of each wave (longitudinal or transverse) scattered by each cylinder expressed with scalar and vector potentials using the Helmholtz decomposition [see Eq. (A1)]. Matrix $\mathcal{T}^{IJ} = \mathcal{T}_p^{IJ}\delta_{pq}$ gathers the individual scattering matrices $\mathcal{T}_p^{IM}$ associated with the cylinder p for an incident wave I and a scattered wave J, they take into account wave conversions and depend on the mechanical properties of the scatterer and on its radius. Matrix $\mathcal{M}^{L,T}$ contains cylindrical harmonics introduced by the use of the addition theorem [23] and vector $\mathcal{F}^{L,T}$ is linked to the incident field which can have an arbitrary polarization or shape, $\mathcal{I}$ is the identity matrix.

Note that the cancellation of the matrix determinant of Eq. (4) leads to the determination of the eigenvalues of the problem, which can be important especially for the calculation of band diagrams of phononic crystals [22,24].
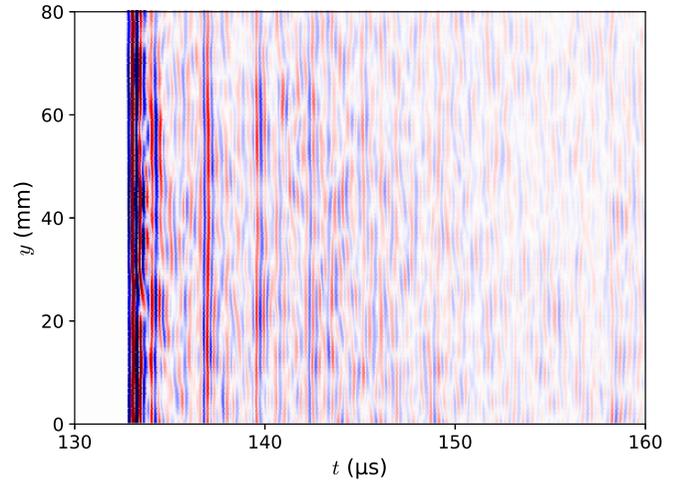

FIG. 5. Map of the transmitted signals through sample 1 as a function of time and lateral position y.

To build the numerical solution, we follow the same steps as those used for MuScat [19]. This linear system (4) can be large and sparse, therefore direct methods are considered inefficient because of their costs in terms of computation time and memory. Iterative methods are more appropriate and a set of these methods is present in the PETSC library (Portable, Extensible Toolkit for Scientific Computation) [25–27], which is chosen to solve the problem. This library works using the parallel MPI (*message passing interface*) architecture, which has the advantage that each processor has its own storage memory. Data communication is performed from one processor to another. The resolution is done with computers that can hold a large number of processors, thus increasing the maximum size of problems if needed. As a conclusion, this resolution method can deal with any situation with many randomly distributed cylinders, combining numerous different scattering matrices and a very large number of scatterers whose properties can fit the framework of this study.

V. COHERENT LONGITUDINAL WAVES

A. Measurement of the effective parameters

The effective wave number k_L^{eff} of coherent longitudinal waves is determined experimentally by measuring the acoustic wave transmission at normal incidence (Fig. 3). The two transducers are laterally translated over 40 positions with increment $\delta y = 1$ mm and the transmitted signal through the sample is acquired. The sample is turned over and 40 others signals are acquired each time. The map of transmitted signals through sample 1 is shown in Fig. 5 as a function of time and lateral positions y. The ballistic wave is clearly dominant and arrives at 134 μs. For each position, few echoes appear after the ballistic wave.

After the acquisition of transmitted signals, the sample is removed from the acoustic path and a reference signal $s_{\mathrm{ref}}(t)$ corresponding to the propagation in a sample made of the same material, without holes and having the same thickness, is acquired. In order to extract the effective properties of the coherent waves, the 80 transmitted signals are averaged. The averaged signal $s_{\mathrm{avg}}(t)$ is compared to the reference signal
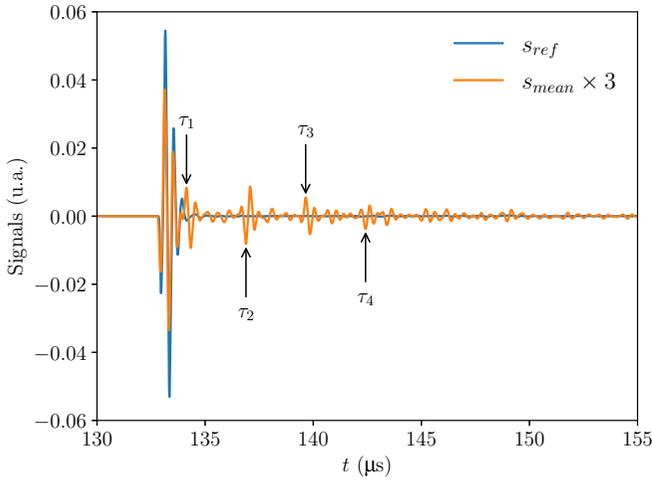
FIG. 6. Averaged signal $s_{\text{avg}}(t)$ and reference signal $s_{\text{ref}}(t)$ as a function of time.

$s_{\text{ref}}(t)$ in Fig. 6. As previously mentioned, few echoes appear after the ballistic wave, with the same shape and duration. Let us denote by τ_i with $i = 1, 2, 3, 4$ the time of flight of the first four echoes appearing in Fig. 6. Using the Hilbert transform of the averaged signal, we evaluate the time of flight difference between two successive echoes: $\Delta\tau = \tau_{i+1} - \tau_i \approx 2, 74 \ \mu s$ for $i = 1, 2, 3$. This duration corresponds to the propagation of a bulk acoustic wave inside a water-filed hole along a distance that is twice the diameter: $\Delta\tau = 4R/c_f = 2, 73 \ \mu s$ [13]. These echoes are therefore identified as several reflections of acoustic wave inside the cavity.

The signals $s_{\text{avg}}(t)$ and $s_{\text{ref}}(t)$ are windowed using an asymmetric Tuckey window. This window starts just before the ballistic wave and ends before the arrival of the second echo in the sample. Thus, due to the large thickness of the samples ($H = 80$ mm), the window duration is large, implying that edge effects are weak. The Fourier transform of the two windowed signals can be expressed as follows:

$$S_{\text{avg}}(f) = A(f)t_{FL}t_{LF}e^{ik_F(\ell-H)}e^{ik_L(H-h)}e^{ik_L^{\text{eff}}h},$$
$$S_{\text{ref}}(f) = A(f)t_{FL}t_{LF}e^{ik_F(\ell-H)}e^{ik_L H}, \tag{5}$$

where the coefficient $A(f)$ represents transduction effects in emission and reception, and t_{FL} and t_{LF} are the transmission coefficients at the water-sample and sample-water interfaces. By calculating the ratio of spectra, the effective phase velocity c_L^{eff} and the attenuation α_L^{eff} of the coherent waves are given by

$$c_L^{\text{eff}} = \frac{\omega h}{k_L h + \arg\left(\frac{S_{\text{avg}}(f)}{S_{\text{ref}}(f)}\right)},$$
$$\alpha_L^{\text{eff}} = -\frac{1}{h}\ln\left|\frac{S_{\text{avg}}(f)}{S_{\text{ref}}(f)}\right|. \tag{6}$$

These parameters are plotted in Fig. 7 as a function of frequency for sample 1, i.e., for a concentration $\phi = 5\%$ of scatterers. Experimental results are compared to ISA and CN models, as well as to the MuScat code. Here ISA refers to the independent scattering approximation. This statistical multiple scattering theory is limited to small concentrations and does not take into account for wave conversions. Error bars
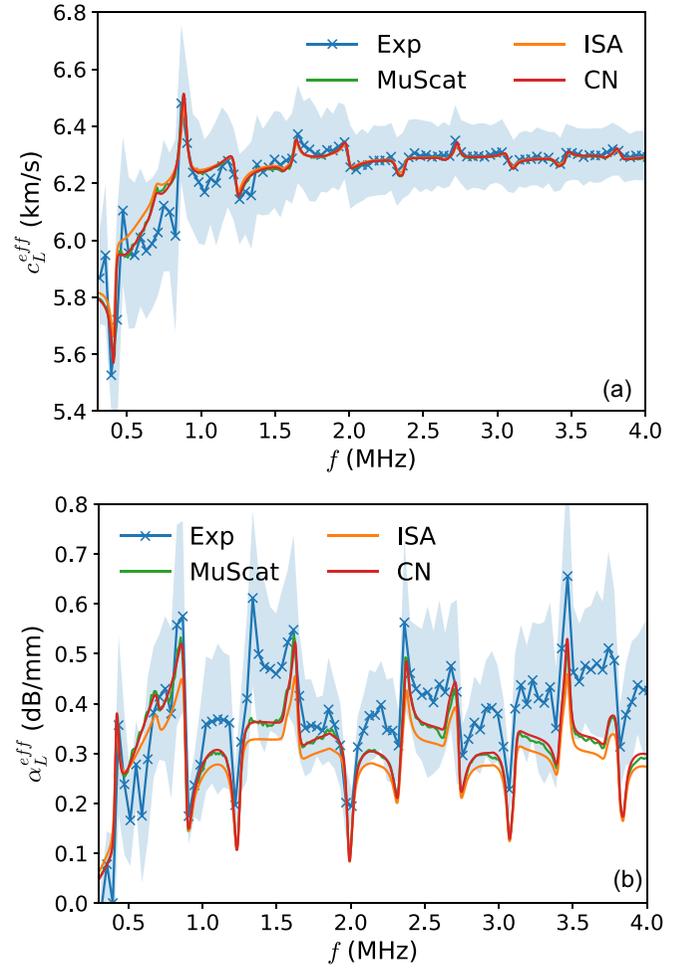

FIG. 7. Effective (a) phase velocity and (b) attenuation of coherent longitudinal waves propagating in sample 1 as a function of frequency.

are difficult to define for such experiments, the standard deviations of the effective phase velocity and attenuation calculated for the 80 signals are displayed instead. The numerical and theoretical results are in good agreement with the experimental data for the phase velocity, but less so for the attenuation. For frequencies $f > 1$ MHz, the attenuation measured is slightly superior to those predicted by the CN model and the MuScat code and even more by that given by ISA. However, results of the CN model are in remarkable agreement with those of MuScat, for both the effective phase velocity and attenuation, the discrepancy with the measured attenuation is maybe due to the sample itself. Indeed, the distribution of scatterers for this sample appears slightly nonhomogeneous (see Fig. 4). The sample being translated after each signal acquisition, the effective concentration, is maybe not the same for all the positions of the sample. Finally, it is worth pointing out that the behavior of the attenuation curves is very similar to that of the normalized scattering cross section γ_{LL}, implying that the influence of wave conversions on the coherent longitudinal wave is weak. Resonances of circumferential waves for $n = 0, 1,$ and 2 have therefore a strong influence on the attenuation. On the contrary, the influence of these resonances
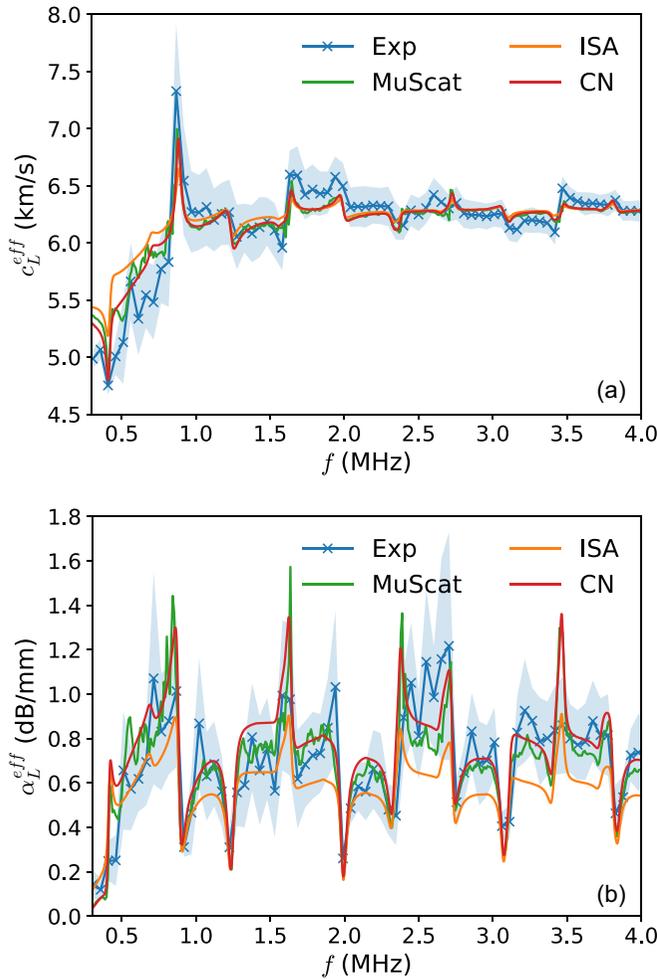
FIG. 8. Effective (a) phase velocity and (b) attenuation of coherent longitudinal waves propagating in sample 2 as a function of frequency.

FIG. 9. Maps of the real part of potentials (a) Φ_L and (b) Φ_T calculated for an incident longitudinal wave. The arrow indicates the propagation direction of the incident plane longitudinal wave and the dashed vertical lines delimit the heterogeneous slab. The color bars are fixed with respect to unit amplitude of the incident wave.

on the phase velocity is stronger for the lowest frequencies, i.e., for $f < 1$ MHz ($k_L R < 1$).

The effective phase velocity and attenuation of coherent longitudinal waves are shown in Fig. 8 for sample 2, i.e., for a concentration $\phi = 9.9\%$ of cavities. As for sample 1, numerical and theoretical results are in quantitative agreement with experimental data. Moreover, ISA underestimates again the attenuation, but the CN model is in better agreement with experiments and numerical simulations. The parameter b/R is equal to 4.75, the distribution of scatterers is more uniform than that of sample 1. This is probably the reason why the standard deviations of the effective phase velocity and attenuation are smaller than those of sample 1.

The CN model has been numerically validated by Chekroun *et al.* in the case of concrete up to a concentration of 25% of scatterers. On the contrary, Yu *et al.* obtained a bad agreement with the CN model compared to experimental results with samples made of a resin containing aluminum rods. In these two studies, the elasticity and mass density contrasts between the two constituents are small, so the scattering effects are relatively weak. In our samples, resonances of water-filled cavities are strong and have an important influence on the coherent waves. Despite this, the CN model
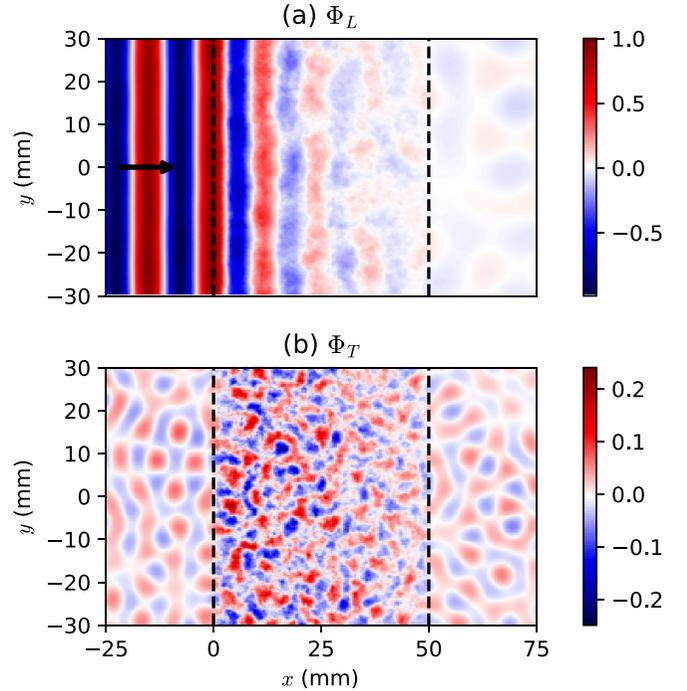
describes very efficiently the propagation of longitudinal coherent waves. Furthermore, the excellent agreement between the numerical results and the CN model validates the use of the exclusion distance b instead of the diameter $2R$ in the CN model. In particular, for the second sample, this exclusion distance is large, the short range correlations are strong and well taken into account by the CN model, without using the pair correlation function.

B. Construction of the coherent longitudinal waves

Numerical simulations are used to observe the construction of the coherent wave. Potentials Φ_L and Φ_T are calculated in a slab of thickness $h = 50$ mm and width $h_t = 300$ mm. The number of cylinders is $N_p = 500$, corresponding to the concentration $\phi = 10.5\%$. The incident plane wave propagates along the x axis. Potentials are averaged over 200 distributions of cylinders. The chosen frequency $f = 424$ kHz corresponds to the resonance of a dipolar mode $n = 1$ as shown by analyzing the scattering cross sections (Fig. 2). This resonance affects both longitudinal and shear waves. For an incident longitudinal wave, the conversion from longitudinal to shear waves is strong ($\gamma_{LT} = 1.6$) and of the same order of magnitude as the scattering of longitudinal waves ($\gamma_{LL} = 2.2$).

The maps of the real part of potentials Φ_L and Φ_T calculated for an incident longitudinal wave of unit amplitude are shown in Figs. 9(a) and 9(b), respectively. The dashed lines delimit the heterogeneous slab. Clearly the propagation of the incident wave is weakly perturbed by the back-scattered waves for $x < 0$ [cf. Fig. 9(a)]. As soon as the incident

wave enters the slab, multiple scattering events occur and the incident wave disappears to make way for the coherent longitudinal plane wave, which is attenuated as it propagates forward in the slab. The potential associated with shear waves in Fig. 9(b) is diffuse, but not small, compared to that of longitudinal waves. This shows that wave conversions have to be taken into account in the modeling of the propagation of longitudinal waves in solid heterogeneous media [28]. Can a longitudinal incident wave generate a coherent shear wave? This is an open question, but our results show that it does not seem to be the case. We indeed observe that even if wave conversions are important, they are not enough to create a shear coherent wave.

C. Poynting vector

As the values of Φ_L and Φ_T can be calculated both inside and outside the slab, the displacement field $\boldsymbol{u}$ can be evaluated thanks to the Helmholtz decomposition (A1). It follows that the Poynting vector can also be calculated everywhere by MuScat. This section aims to present results about the component of the Poynting vector in the propagation direction in order to observe how it decreases into the slab.

The component of the Poynting vector along the propagation direction of the plane incident wave, i.e., the x direction, is defined by the relation

$$P_x = \frac{1}{2}\,\mathrm{Re}\,[\boldsymbol{\sigma}\cdot\boldsymbol{u}^\star]\cdot\boldsymbol{e}_x = -\frac{\omega}{2}[i\sigma_{xx}u_x^\star + i\sigma_{xy}u_y^\star], \quad (7)$$

where stresses are related to displacements by Hooke's law

$$\sigma_{xx} = (\lambda + 2\mu)\frac{\partial u_x}{\partial x} + \lambda\frac{\partial u_y}{\partial y},$$

$$\sigma_{xy} = \mu\left(\frac{\partial u_x}{\partial y} + \frac{\partial u_y}{\partial x}\right). \quad (8)$$

These stresses and the displacement components are averaged over 200 distributions of scatterers. The averaged component P_x is calculated along the x axis, using these averaged stresses and displacement components and is then averaged over the position y. The component $\langle P_x \rangle_y$ normalized by its value at $x = 0$ is plotted as a function of position x in Fig. 10 for frequencies $f = 1$, 2, 3, and 3.5 MHz in the case of an incident longitudinal wave. Numerical parameters are the same as those used in Sec. V B, except that the concentration is $\phi = 5.2\%$. It is worth noting that the averaged component $\langle P_x \rangle_y$ does not start to decrease at $x = 0$, but approximately at $x = 2R$. It implies that the coherent wave does not take the place of the incident wave at the beginning of the heterogeneous slab, but only after at least one event of scattering. The use of the thickness h in the treatment of the previous section to obtain the effective wave number is therefore debatable and the use of an effective "width" $h_{\mathrm{eff}} \approx h - 2R$ instead of h remains an open question [29]. In order to interpret these results, we assume that the normalized component $\langle P_x \rangle_y$ is given by the Beer-Lambert law [30]

$$\frac{\langle P_x(x,y)\rangle_y}{\langle P_x(x=0,y)\rangle_y} = e^{-2\alpha_L^{\mathrm{eff}}x}. \quad (9)$$
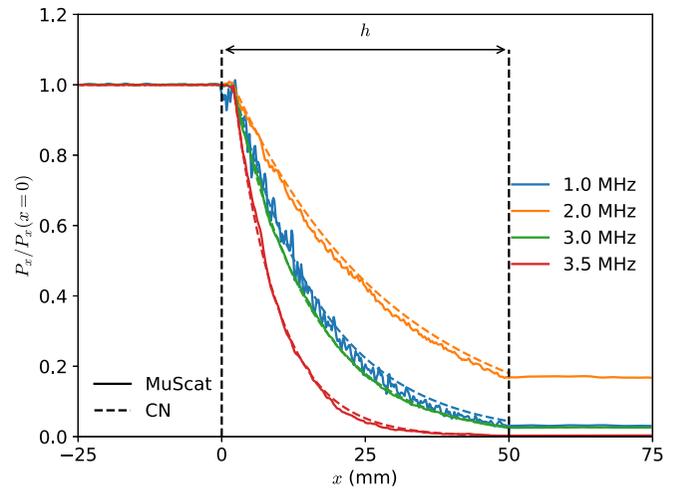

FIG. 10. Component of the Poynting vector in the direction of propagation as a function of the position x.

Dashed curves in Fig. 10 correspond to this expression by using the attenuation α_L^{eff} given by the CN model. For highest frequencies, namely $f = 3$ and 3.5 MHz, the Beer-Lambert law with the CN model is in quantitative agreement with numerical results. This result is not trivial because the component P_x is calculated in an exact way by MuScat, i.e., from the displacements, while P_x, which is modeled using the Beer-Lambert law and the CN model, involves only the knowledge of the potentials in order to calculate α_L^{eff}.

VI. COHERENT SHEAR WAVES

A. Measurement of the effective parameters

Shear wave measurements are often performed using contact transducers that need to use coupling materials to efficiently transmit waves in the samples. Such couplings are difficult to reproduce, we chose to adapt the immersion technique used for longitudinal wave measurements to oblique incidence in order to convert longitudinal acoustic waves to shear waves. The main advantage is that liquid wetting ensures a reproducible transmission at the liquid-sample and sample interfaces. Moreover, using angle of incidence beyond the critical angle allows us to generate by refraction only a shear traveling wave in the sample [31]. Two transducers are placed on either side of the sample to be probed. The incident wave propagates in water with the angle of incidence θ_F from the normal of the front surface of the sample (Fig. 11). By imposing an angle $\theta_F = 20°$ larger than the first critical angle $\arcsin(c_F/c_L) \approx 13.6°$, the interaction of the incident wave with this liquid-solid interface gives rise to a single shear wave propagating in the sample with the angle of incidence $\theta_T = 45.2°$. The value of the angle of incidence θ_F is chosen to maximize the wave transmission through the two interfaces of the front and back sides of the sample. The length of the acoustic path in the sample is $\tilde{H} = H/\cos\theta_T = 11,3$ cm. The acoustic beam in the sample is deviated by refraction, the receiver is translated laterally of a distance $\delta = \tilde{H}\sin(\theta_T - \theta_F) = 4,8$ cm.
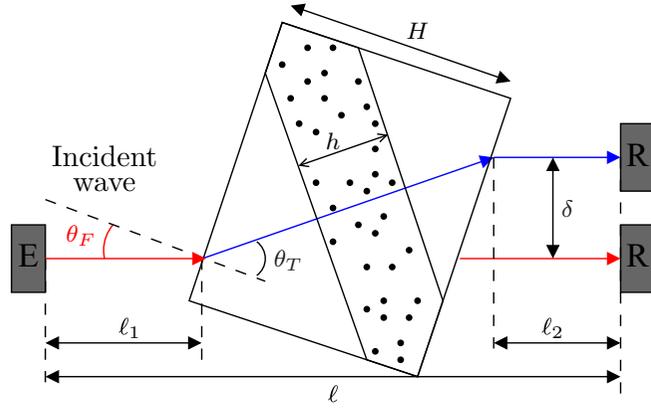
FIG. 11. Scheme of the experiment for measuring the coherent shear wave.

The transmitted signal through the sample is averaged over 30 positions. The Fourier transforms of the averaged signal and of the reference signal in a sample without holes are expressed by

$$S_{\text{avg}}(f) = A(f) t_{FT} t_{TF} e^{ik_F(\ell_1+\ell_2)} e^{ik_T(\tilde{H}-h)} e^{ik_T^{\text{eff}} h},$$

$$S_{\text{ref}}(f) = A(f) t_{FT} t_{TF} e^{ik_F(\ell_1+\ell_2)} e^{ik_T \tilde{H}}, \tag{10}$$

where t_{FT} and t_{TF} are the transmission coefficients at the water-aluminum alloy and aluminum alloy-water interfaces. The ratio of these spectra leads to the expressions of the effective phase velocity c_T^{eff} and attenuation α_T^{eff} given by the relations (6) in which k_L is replaced by k_T.

These effective parameters are shown in Fig. 12 for sample 3, i.e., for a concentration $\phi = 7.1\%$ of scatterers. As for the longitudinal case, these results are compared to those obtained by ISA, the CN model, and the MuScat code. Resonances of the circumferential waves therefore strongly impact the effective phase velocity and attenuation of the coherent shear waves. The attenuation curves have by the way the same behavior as that of the scattering cross section γ_{TT} in Fig. 1(a). From 1 to 3 MHz, the CN model is in quantitative agreement with numerical and experimental results. The sample is tilted, the distance ℓ between transducers is larger than for the normal incidence measurements. Experimental results are therefore potentially influenced by diffraction effects due to the beam divergence in the lowest frequencies. In highest frequencies, the attenuation predicted by ISA has the same behavior as those of experimental results, but its mean value is smaller. This effect is less pronounced for the attenuation given by the CN model and MuScat. Thus, as in the case of the longitudinal coherent wave, the CN model is validated experimentally and numerically for modeling coherent shear waves in two-dimensional multiple scattering media.

B. Construction of the coherent shear waves

The maps of the real part of potentials Φ_L and Φ_T calculated for an incident shear wave of unit amplitude are shown in Figs. 13(a) and 13(b), respectively. Results are very similar to those of Fig. 9. The potential associated with longitudinal waves in Fig. 13(b) is not small, compared to that of shear
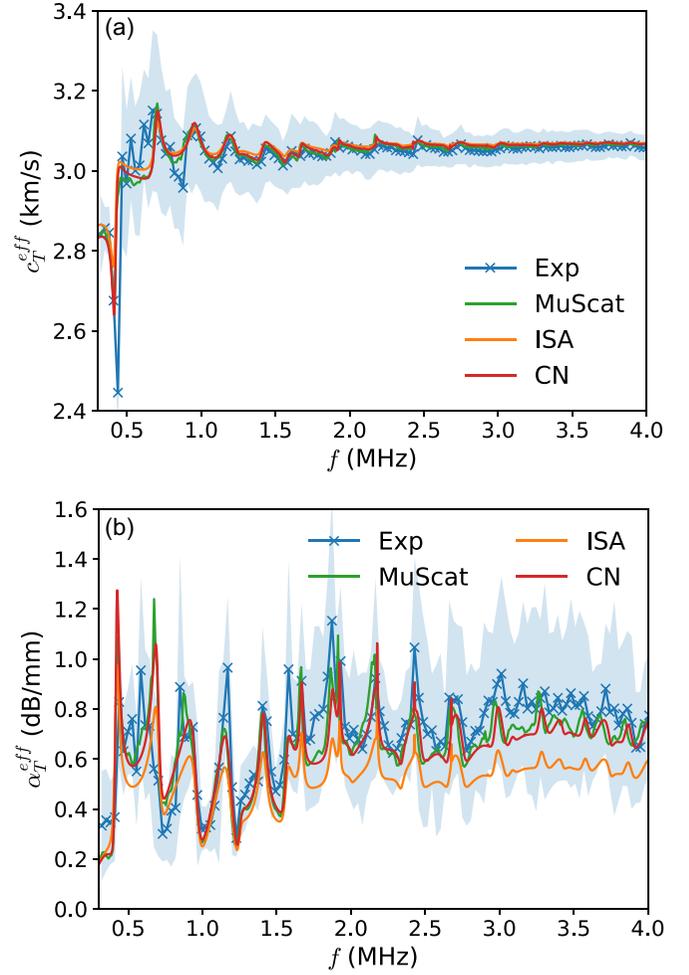

FIG. 12. Effective (a) phase velocity and (b) attenuation of coherent shear waves propagating in sample 3 as a function of frequency.

waves. The scattering cross section $\gamma_{TL} = 0.8$ is small compared to $\gamma_{TT} = 4.6$, we could expect a weak influence of wave conversions on coherent shear waves. This is not the case because of the multiple scattering. This result is quite surprising and reinforces the idea that wave conversions have to be taken into account in the modeling of elastic waves propagating in solid heterogeneous media, even for shear incident waves. Nevertheless, we can make the same remark as previously, namely that an incident shear wave does not generate a coherent longitudinal wave which would be detectable.

VII. CONCLUSION

Propagation of coherent elastic waves in solids containing strong resonant cylindrical scatterers has been studied numerically and experimentally.

Numerical modeling is based on the semianalytical solution of multiple scattering, where incident and scattered waves are expanded on cylindrical harmonics. This modeling, initially derived for fluid hosts, has been adapted for solid cases and thus takes into account wave conversions at the surface of each scatterer. Numerical results highlights the influence of wave conversions in the low frequency regime on the coherent
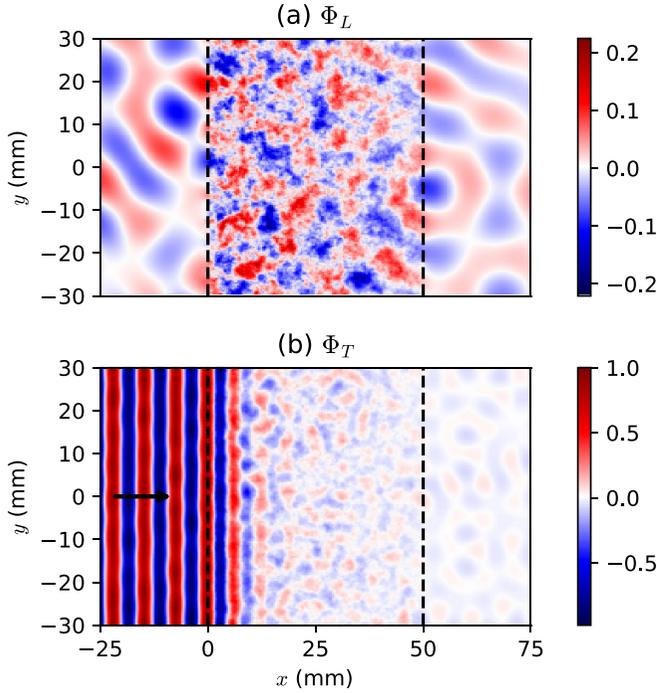
FIG. 13. Maps of the real part of potentials (a) Φ_L and (b) Φ_T calculated for an incident shear wave. The arrow indicates the propagation direction of the incident plane shear wave and the dashed vertical lines delimit the heterogeneous slab. The color bars are fixed with respect to unit amplitude of the incident wave.

elastic waves and the necessity to take them into account in solid heterogeneous media. It has been shown that an incident longitudinal wave does not generate a coherent shear wave. In this case, no constructive interference is observed between the bulk shear waves so that the transverse component of the coherent wave exists but remains diffusive. Constructive interference occurs only for longitudinal bulk waves. Similarly, an incident shear wave does not generate a coherent longitudinal wave. It has also been shown that the Poynting vector calculated by MuScat obeys the Beer-Lambert law in which the attenuation is calculated from the CN homogenization model.

Coherent wave measurements have also been performed in transmission at normal incidence for longitudinal waves and at oblique incidence beyond the critical angle for shear waves. The originality of the shear wave measurements is that they are carried out in water; the conversion at the water-solid interface is used to generate shear waves in the multiple scattering medium. Measurements highlighted the strong influence of the resonances on the coherent waves. Remarkable agreements between results up to a 9.9% of scatterers for longitudinal waves and 7.1% for shear waves highlight the efficiency of both the Conoir-Norris model and the MuScat code to predict coherent elastic waves.

Since the MuScat code can handle a large number of cylinders randomly distributed in space, many studies are possible as the transition from ballistic to diffusive regimes for elastic waves [32] or the propagation of elastic waves in dense materials [33] or stealth hyperuniform materials [34,35].

APPENDIX: DERIVATION OF THE NUMERICAL MODEL

Let us consider the cartesian coordinate system $\mathbb{R} = (O, x, y, z)$. Our study is restricted to the plane (x, y). As the cylinders are all parallel to the z axis, it follows that only longitudinal and shear vertical waves propagate in the solid. For the sake of simplicity, the time dependence $e^{-i\omega t}$ is omitted throughout the text. We assume the Helmholtz decomposition of the displacement in the form

$$\boldsymbol{u} = \mathbf{grad}\ \Phi_L + \mathbf{rot}\ (\Phi_T \boldsymbol{e}_z), \tag{A1}$$

where the potentials Φ_L and Φ_T are associated, respectively, with longitudinal (L) and shear waves (T) are solutions to the Helmholtz equation:

$$\Delta \Phi_M + k_M^2 \Phi_M = 0, \tag{A2}$$

where $M = L, T$ designates the nature of the waves. It is worth noting that the shear wave, whose polarization is parallel to cylinders, is not retained because it is decoupled to the L and T waves, polarized in the (x, y) plane.

The host solid contains a distribution of N_p parallel, infinite cylinders of radius R_p that do not interpenetrate. An arbitrary coordinate system $\mathbb{R}_0$ is defined to describe the propagation of the incident wave and each scatterer p is associated with a coordinate system $\mathbb{R}_p$ whose origin coincides with its center. Generally speaking, two incident longitudinal and shear waves can propagate in the matrix; their potential in the coordinate system $\mathbb{R}_0$ are expanded on cylindrical harmonics:

$$\Phi_{(\text{inc},M)}(\boldsymbol{x}_0) = [\psi(k_M, \boldsymbol{x}_0)]^t \mathcal{A}^M, \tag{A3}$$

where the superscript t stands for the transpose of a vector and with

$$\psi_n(k, \boldsymbol{x}) = J_n(kr)e^{in\theta}, \tag{A4}$$

where J_n is the Bessel function of the first kind and order n. The vector $\mathcal{A}^M$ depends on the kind of incident wave, i.e., plane wave, source point, Gaussian beam, etc. It has N_m components, with N_m the number of modes taken into account that increases with the frequency.

The potentials $\Phi_{(\text{scat},M)}$ associated with the scattered longitudinal or shear waves are the sum of the fields scattered by each cylinder:

$$\Phi_{(\text{scat},M)} = \sum_{p=1}^{N_p} \Phi_M^p(\boldsymbol{x}_p). \tag{A5}$$

As for the incident wave, the potential of the scattered wave by each cylinder is expanded on cylindrical harmonics

$$\Phi_M^p(\boldsymbol{x}_p) = [\chi(k_M, \boldsymbol{x}_p)]^t \mathcal{B}_p^M, \tag{A6}$$

with

$$\chi_n(k, \boldsymbol{x}_p) = H_n(kr_p)e^{in\theta_p}, \tag{A7}$$

where $H_n \equiv H_n^{(1)}$ is the Hankel function of the first kind and order n. The components of the vector $\mathcal{B}_p^M$ are the unknowns of the problem. The incident field on the cylinder p corresponds to the incident wave represented by $\Phi_{(\text{inc},M)}$ and the

scattered waves by all the other cylinders, namely

$$\Phi^p_{(\text{inc},M)} = \Phi_{(\text{inc},M)}(\boldsymbol{x}_0) + \sum_{\substack{q=1 \\ q \neq p}}^{N_p} \Phi^q_M(\boldsymbol{x}_q) \tag{A8}$$

or, using cylindrical harmonics expansions (A3) and (A6),

$$\Phi^p_{(\text{inc},M)} = [\psi(k_M, \boldsymbol{x}_0)]^t \mathcal{A}^M + \sum_{\substack{q=1 \\ q \neq p}}^{N_p} [\chi(k_M, \boldsymbol{x}_q)]^t \mathcal{B}^M_q. \tag{A9}$$

This expression of the potential $\Phi^p_{(\text{inc},M)}$ involves several coordinate systems. All potentials are then expressed in the coordinate system $\mathbb{R}_p$ associated with the p cylinder. To do this, let us define a point P, marked by the position vectors $\boldsymbol{x}_i$ and $\boldsymbol{x}_j$ in the coordinate systems $\mathbb{R}_i$ and $\mathbb{R}_j$, respectively. The vector $\boldsymbol{x}_{ij}$ describes the position of the point O_j in the coordinate system $\mathbb{R}_i$. Using the Graf's addition theorem, cylindrical harmonics at the position $\boldsymbol{x}_i$ in the coordinate system $\mathbb{R}_i$ can be expressed as a function of cylindrical harmonics at the position $\boldsymbol{x}_j$ in the coordinate system $\mathbb{R}_j$ thanks to the relations [23]

$$[\chi(k, \boldsymbol{x}_i)]^t = [\psi(k, \boldsymbol{x}_j)]^t \mathcal{M}(k, \boldsymbol{x}_{ij}),$$
$$[\psi(k, \boldsymbol{x}_i)]^t = [\psi(k, \boldsymbol{x}_j)]^t \mathcal{N}(k, \boldsymbol{x}_{ij}), \tag{A10}$$

with

$$\mathcal{M}_{\nu n}(k, \boldsymbol{x}_{ij}) = \chi_{n-\nu}(k, \boldsymbol{x}_{ij}),$$
$$\mathcal{N}_{\nu n}(k, \boldsymbol{x}_{ij}) = \psi_{n-\nu}(k, \boldsymbol{x}_{ij}). \tag{A11}$$

Using these relations, the potential of the incident wave on the cylinder p can be put in the form

$$\Phi^p_{(\text{inc},M)}(\boldsymbol{x}_p) = [\psi(k_M, \boldsymbol{x}_p)]^t \mathcal{C}^M_p, \tag{A12}$$

with

$$\mathcal{C}^M_p = \mathcal{N}(k_M, \boldsymbol{x}_{0p}) \mathcal{A}^M + \sum_{\substack{q=1 \\ q \neq p}}^{N_p} \mathcal{M}(k_M, \boldsymbol{x}_{qp}) \mathcal{B}^M_q. \tag{A13}$$

Amplitudes of incident waves are linked to those of the scattered waves are by the relation

$$\mathcal{B}^M_p = \sum_{I=L,T} \mathcal{T}^{IM}_p \mathcal{C}^I_p, \tag{A14}$$

where $\mathcal{T}^{IM}_p$ is the scattering matrix associated with the cylinder p for an incident wave I and a scattered wave M. This matrix is diagonal whose coefficients are the scattering coefficients T^{IM}_{pn}. These coefficients are calculated independently for each scatterer, they take into account wave conversions and depend on the mechanical properties of the scatterer and on its radius.

Let us define the vectors $\mathcal{F}^M$ and the matrices $\mathcal{T}^{M_1 M_2}$ and $\mathcal{M}^M$ as follows:

$$\mathcal{F}^M_p = \mathcal{N}(k_M, \boldsymbol{x}_{0p}) \mathcal{A}^M,$$
$$\mathcal{T}^{M_1 M_2}_{pq} = \mathcal{T}^{M_1 M_2}_p \delta_{pq},$$
$$\mathcal{M}^M_{pq} = \mathcal{M}(k_M, \boldsymbol{x}_{qp})(1 - \delta_{pq}). \tag{A15}$$

We finally obtain the set of equations:

$$\mathcal{B}^L = \sum_{M=L,T} \mathcal{T}^{ML}(\mathcal{F}^M + \mathcal{M}^M \mathcal{B}^M),$$
$$\mathcal{B}^T = \sum_{M=L,T} \mathcal{T}^{MT}(\mathcal{F}^M + \mathcal{M}^M \mathcal{B}^M), \tag{A16}$$

which can be recast into a matrix/vector form [see Eq. (4)].

[1] S. Bose and A. Mal, Elastic waves in a fiber-reinforced composite, J. Mech. Phys. Solids **22**, 217 (1974).

[2] R.-B. Yang and A. K. Mal, Multiple scattering of elastic waves in a fiber-reinforced composite, J. Mech. Phys. Solids **42**, 1945 (1994).

[3] S. Rokhlin, W. Huang, and Y. Chu, Ultrasonic scattering and velocity methods for characterization of fibre-matrix interphases, Ultrasonics **33**, 351 (1995).

[4] J. Mei, Z. Liu, W. Wen, and P. Sheng, Effective dynamic mass density of composites, Phys. Rev. B **76**, 134205 (2007).

[5] F. Liu and Z. Liu, Elastic Waves Scattering without Conversion in Metamaterials with Simultaneous Zero Indices for Longitudinal and Transverse Waves, Phys. Rev. Lett. **115**, 175502 (2015).

[6] J. Conoir and A. N. Norris, Effective wavenumbers and reflection coefficients for an elastic medium containing random configurations of cylindrical scatterers, Wave Motion **47**, 183 (2010).

[7] M. Chekroun, L. Le Marrec, B. Lombard, and J. Piraux, Time-domain numerical simulations of multiple scattering to extract elastic effective wavenumbers, Waves in Random and Complex Media **22**, 398 (2012).

[8] T. Yu, J.-F. Chaix, L. Audibert, D. Komatitsch, V. Garnier, and J.-M. Hénault, Simulations of ultrasonic wave propagation in concrete based on a two-dimensional numerical model validated analytically and experimentally, Ultrasonics **92**, 21 (2019).

[9] A. Simon, R. Wunenburger, and T. Valier-Brasier, Propagation of coherent shear waves in scattering elastic media, Phys. Rev. E **103**, L051001 (2021).

[10] M. L. Cowan, K. Beaty, J. H. Page, Z. Liu, and P. Sheng, Group velocity of acoustic waves in strongly scattering media: Dependence on the volume fraction of scatterers, Phys. Rev. E **58**, 6626 (1998).

[11] B. Tallon, T. Brunet, and J. Page, Impact of Strong Scattering Resonances on Ballistic and Diffusive Wave Transport, Phys. Rev. Lett. **119**, 164301 (2017).

[12] B. Tallon, T. Brunet, J. Leng, and J. H. Page, Energy velocity of multiply scattered waves in strongly scattering media, Phys. Rev. B **101**, 054202 (2020).

[13] Y. Pao and W. Sachse, Interpretation of time records and power spectra of scattered ultrasonic pulses in solids, J. Acoust. Soc. Am. **56**, 1478 (1974).

[14] Y. Pao and C. Mow, Theory of normal modes and ultrasonic spectral analysis of the scattering of waves in solids, J. Acoust. Soc. Am. **59**, 1046 (1976).

[15] W. Hassan and P. B. Nagy, Circumferential creeping waves around a fluid-filled cylindrical cavity in an elastic medium, J. Acoust. Soc. Am. **101**, 2496 (1997).

[16] L. Tsang, J. A. Kong, and K.-H. Ding, *Scattering of Electromagnetic Waves: Theories and Applications* (John Wiley and Sons, New York, 2000).

[17] Y. Liu, R. Wu, and C. F. Ying, Scattering of elastic waves by an elastic or viscoelastic cylinder, Geophys. J. Int. **142**, 439 (2000).

[18] F. Zàviška, Über die Beugung elektromagnetischer Wellen an parallelen, unendlich langen Kreiszylindern, Ann. Phys. (Berlin) **345**, 1023 (1913).

[19] A. Rohfritsch, J.-M. Conoir, R. Marchiano, and T. Valier-Brasier, Numerical simulation of two-dimensional multiple scattering of sound by a large number of circular cylinders, J. Acoust. Soc. Am. **145**, 3320 (2019).

[20] A. Rohfritsch, J.-M. Conoir, T. Valier-Brasier, and R. Marchiano, Influence of the microstructure of two-dimensional random heterogeneous media on propagation of acoustic coherent waves, Phys. Rev. E **101**, 023001 (2020).

[21] A. Rohfritsch, J.-M. Conoir, T. Valier-Brasier, and R. Marchiano, Impact of particle size and multiple scattering on the propagation of waves in stealthy-hyperuniform media, Phys. Rev. E **102**, 053001 (2020).

[22] J. Mei, Z. Liu, J. Shi, and D. Tian, Theory for elastic wave scattering by a two-dimensional periodical array of cylinders: An ideal approach for band-structure calculations, Phys. Rev. B **67**, 245107 (2003).

[23] P. Martin, *Multiple Scattering - Interaction of Time-Harmonic Waves with N Obstacles* (Cambridge University Press, Cambridge, 2006).

[24] C. Qiu, Z. Liu, J. Mei, and M. Ke, The layer multiple-scattering method for calculating transmission coefficients of 2D phononic crystals, Solid State Commun. **134**, 765 (2005).

[25] S. Balay, S. Abhyankar, M. F. Adams, J. Brown, P. Brune, K. Buschelman, L. Dalcin, A. Dener, V. Eijkhout, W. D. Gropp, D. Kaushik, M. G. Knepley, D. A. May, L. C. McInnes, R. T. Mills, T. Munson, K. Rupp, P. Sanan, B. F. Smith, S. Zampini, H. Zhang, and H. Zhang, PETSc Web page, http://www.mcs.anl.gov/petsc, 2018.

[26] S. Balay, S. Abhyankar, M. F. Adams, J. Brown, P. Brune, K. Buschelman, L. Dalcin, A. Dener, V. Eijkhout, W. D. Gropp, D. Kaushik, M. G. Knepley, D. A. May, L. C. McInnes, R. T. Mills, T. Munson, K. Rupp, P. Sanan, B. F. Smith, S. Zampini, H. Zhang, and H. Zhang, PETSc users manual, Technical Report No. ANL-95/11 - Revision 3.10, Argonne National Laboratory (unpublished).

[27] S. Balay, W. D. Gropp, L. C. McInnes, and B. F. Smith, Efficient management of parallelism in object oriented numerical software libraries, in *Modern Software Tools in Scientific Computing*, edited by E. Arge, A. M. Bruaset, and H. P. Langtangen (Birkhäuser, Basel, 1997), pp. 163–202.

[28] M. Duranteau, T. Valier-Brasier, J.-M. Conoir, and R. Wunenburger, Random acoustic metamaterial with a subwavelength dipolar resonance, J. Acoust. Soc. Am. **139**, 3341 (2016).

[29] S. Durant, O. Calvo-Perez, N. Vukadinovic, and J.-J. Greffet, Light scattering by a random distribution of particles embedded in absorbing media: Full-wave monte carlo solutions of the extinction coefficient, J. Opt. Soc. Am. A **24**, 2953 (2007).

[30] A. Ishimaru, *Wave Propagation and Scattering in Random Media. Volume 2 Multiple Scattering, Turbulence, Rough Surfaces, and Remote Sensing* (Academic, New York, 1978).

[31] J. Wu, Determination of velocity and attenuation of shear waves using ultrasonic spectroscopy, J. Acoust. Soc. Am. **99**, 2871 (1996).

[32] Z. Q. Zhang, I. P. Jones, H. P. Schriemer, J. H. Page, D. A. Weitz, and P. Sheng, Wave transport in random media: The ballistic to diffusive transition, Phys. Rev. E **60**, 4843 (1999).

[33] M. L. Cowan, J. H. Page, and P. Sheng, Ultrasonic wave transport in a system of disordered resonant scatterers Propagating resonant modes and hybridization gaps, Phys. Rev. B **84**, 094305 (2011).

[34] G. Gkantzounis, T. Amoah, and M. Florescu, Hyperuniform disordered phononic structures, Phys. Rev. B **95**, 094120 (2017).

[35] J. Kim and S. Torquato, Multifunctional composites for elastic and electromagnetic wave propagation, Proc. Natl. Acad. Sci. U.S.A. **117**, 8764 (2020).